SOFT ROBOTS

Highly agile flat swimming robot

Florian Hartmann[1,2]*, Mrudhula Baskaran[3], Gaetan Raynaud[3], Mehdi Benbedda[1]†, Karen Mulleners[3], Herbert Shea[1]*

Navigating and exploring the surfaces of bodies of water allow swimming robots to perform a range of measurements while efficiently communicating and harvesting energy from the Sun. Such environments are often highly unstructured and cluttered with plant matter, animals, and debris, which require robots to move swiftly. We report a fast (5.1 centimeters per second translation and 195 degrees per second rotation), centimeter-scale swimming robot with high maneuverability and autonomous untethered operation. Locomotion is enabled by a pair of soft, millimeter-thin, undulating pectoral fins, in which traveling waves are electrically excited to generate propulsion. The actuators, robot design, and power supply are codesigned to enable high-performance locomotion in a scaled-down system. A single soft electrohydraulic actuator per side generates the traveling wave. A compact and lightweight power supply enables untethered operation, made possible by decreasing the operating voltage of the electrohydraulic actuators to below 500 volts and their power consumption to 35 milliwatts. By an experimental study and by modeling, we determined optimum dimensions and operating conditions across designs and size scales. The robots navigate through narrow spaces and through grassy plants and push objects weighing more than 16 times their body weight. Such robots can allow exploration of complex environments as well as continuous measurement of plant and water parameters for aquafarming.

INTRODUCTION

Aquatic robots explore bodies of water and the plant and animal life they contain. Swimming robots enable mapping of water pollution (*1*), research in marine biology (*2*), and deep-sea exploration (*3*). Harnessing biomimicry has enabled these robots to blend into natural environments through silent and life-like locomotion. However, the sizes (>30 cm), weights (>1 kg), or propulsion strategies of those robots confine them to open and uncluttered underwater environments (*2*–*7*). Operating on the water surface allows accessing both water and air for measurements while simultaneously permitting communication with terrestrial or aerial infrastructure and energy harvesting from the Sun. Harmlessly interacting with—or avoiding—animals, plants, or organic and plastic debris requires small and light robots capable of agile movements. Scenarios such as swimming through a rice field or performing inspection through narrow openings benefit from centimeter-scale (1 to 10 cm) robots. Inspired by water striders, rays, or amphibians, scientists have built a diverse set of centimeter-scale swimmers that walk (*8*–*10*), glide (*11*–*13*), and row on water (*14*–*16*) or use vibrations (*17*–*19*) or undulations (*20*–*25*) for locomotion. Most of these devices cannot maneuver or are tethered to an external power supply, limiting their applicability. Untethered operation of centimeter-scale robots requires millimeter-to-centimeter–scale actuators, which must provide sufficient thrust for propulsion when driven by a lightweight onboard power supply. Actuations based on electro-osmotic hydrogels (*14*) or miniature dc motors (*10*, *19*) are possible avenues for maneuverable, untethered swimmers, but they show moderate agility, use fragile rudders, or are bulky, and none can navigate autonomously.

Here, we introduce a family of centimeter-scale (25- to 45-mm length), fast (12 cm/s tethered and 5.1 cm/s untethered), and maneuverable (120°/s tethered and 195°/s untethered) soft swimming robots with autonomous operation in both energy and trajectory. Propulsion comes from traveling waves that are excited along a pair of undulating pectoral fins on the water surface, similar to polyclads—marine flatworms. The robot consists of a flat submillimeter-thin locomotion module (actuators and undulating fins) and a printed circuit board (PCB) with the power supply, control, optical sensing, and communication electronics (Fig. 1A). The locomotion modules monolithically integrate a pair of soft undulating fins with soft electrohydraulic actuators that operate at voltages below 500 V, at low power (<35 mW), and at high bandwidth (>100 Hz) and that are durable (more than 750,000 actuation cycles). An experimental and analytic study of the influence of robot dimensions on the ideal operation conditions allows us to optimize designs at different scales. Modular design strategies extend locomotion capabilities beyond forward swimming and turning to include backward and sideways swimming, offering versatile operation similar to quadcopters in air. We demonstrate autonomous and untethered operation on the water surface facilitated by the integration of sensors (for both infrared and visible light), energy supply, power conversion, and control. The swimming robots circumnavigate obstacles, swim through narrow spaces, and push away objects with 16 times their own body weight, enabling practical tasks through high thrust generation. They detect moving or stationary light sources and navigate toward or away from them. This agile robotic swimmer combines advances in propulsion performance, robustness, and functionality and will help to inspire future miniaturized vehicles operating in natural aquatic environments.

[1]Soft Transducers Laboratory (LMTS), École Polytechnique Fédérale de Lausanne (EPFL), Neuchâtel, Switzerland. [2]Biomimetic Materials and Machines Group, Max Planck Institute for Intelligent Systems, Stuttgart, Germany. [3]Unsteady Flow Diagnostics Laboratory, EPFL, Lausanne, Switzerland.
*Corresponding author. Email: hartmann@is.mpg.de (F.H.); herbert.shea@epfl.ch (H.S.)
†Present address: Helbling Technik Bern AG, Liebefeld-Bern, Switzerland.

RESULTS

Locomotion and robot design

We designed a robot architecture that fulfills four requirements: first, versatile locomotion capabilities, including directional swimming and turning; second, facile integration of PCBs to allow untethered

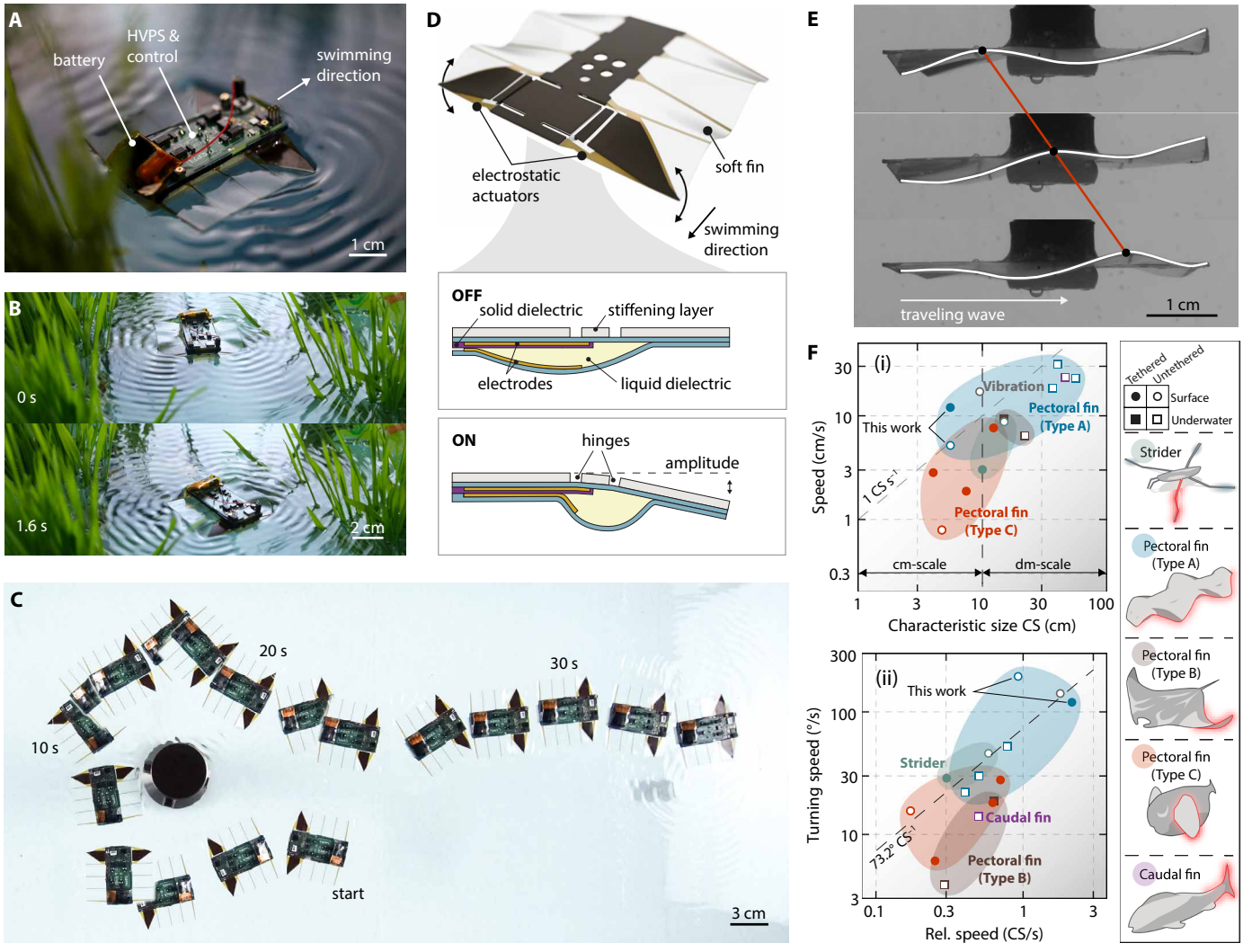

Fig. 1. Untethered highly agile flat robots evolving in aquatic environments. (**A**) Untethered and autonomous robot (length, 45 mm) including miniaturized HVPS and onboard control electronics. Scale bar, 1 cm. (**B**) Robot swimming on the water surface in a cluttered environment. Scale bar, 2 cm. (**C**) Individual control of the actuators allows controlled navigation of the robot, enabling turns to the left or right or swimming forward. Scale bar, 3 cm. (**D**) Schematic of a flat locomotion module using two electrohydraulic actuators to drive a pair of undulating soft pectoral fins. (**E**) Applying a periodic high-voltage signal leads to oscillatory bending motion of electrohydraulic actuators and, hence, the generation of a traveling wave along the soft fins, both underwater and on the water surface. Scale bar, 1 cm. (**F**) Performance comparison of maneuverable swimming robots. Our centimeter-scale robots show high agility and speed relative to the robot's CS. Shaded areas mark bioinspired locomotion modes for underwater, water surface, tethered, and untethered swimmers. (i) The dashed line marks a relative speed of 1 CS/s. (ii) The dashed line marks a linear fit of the represented data, with a slope of 73.2°/CS. Points above this line have more efficient rotation compared with the average robot.

operation; third, locomotion design with reduced complexity using the minimal number of actuators; and fourth, a small footprint to allow navigation through narrow spaces (~5 cm) in natural environments. We addressed these requirements by developing a robot that is based on a flat locomotion module (~500-μm-thick), inspired by marine flatworms like Pseudocerotidae, featuring a pair of undulating pectoral fins on its sides. For flatworms, the fins extend longitudinally along the entire body and generate multiple traveling waves along the fin, aiding in locomotion and stability (*26*). Similar to its natural counterpart, we realized a locomotion mode with more than 1.5 wavelengths along the fin (fig. S1), larger than in most other artificial, small-scale swimmers based on undulatory pectoral fins.

In contrast with most marine animals and robots, the locomotion module floats on the water surface because of surface tension, benefiting from a high surface area, and can carry larger weights when combined with buoyant elements. Undulation of the fins generated flow both on the water surface and beneath, resulting in propulsion. Through the individual control of each fin, we achieved high maneuverability, enabling forward locomotion and turns using only two actuators (Fig. 1, B and C). Compared with larger marine robots, which typically require multiple (6 to 14) actuators and complex control to drive undulating fins (*6*, *7*), this minimal use of actuators reduced power consumption while maintaining the full richness of the undulating motion. In our robot, each fin was driven by a single,

monolithically integrated, soft electrohydraulic actuator, powered and controlled by the onboard electronics. We designed a miniaturized multichannel high-voltage power supply (HVPS), supplying two bipolar 600-V signals from a 35 mm–by–20 mm PCB. Downlink communication through infrared sensors or ambient light phototransistors, computing, and energy storage completed the circuit, allowing autonomous and untethered operation.

We chose soft electrohydraulic actuators because of their high performance, direct electric controllability, scalability, and extremely low acoustic noise (*4*, *27*). Soft electrohydraulic actuators are a class of capacitive transducers that convert a high-voltage input into motion. The capacitive architecture comprised two electrodes, which were separated by layers of solid and liquid dielectrics. When an electric field was applied, the electrodes zipped together because of Maxwell stress and displaced the liquid dielectric, which was used for deformation of the actuator (Fig. 1D). The force output depended primarily on the applied voltage and on the thickness and permittivity of the dielectric layers. The range of motion depended on the actuator geometry and the amount of liquid that was filled into the pouches, given that the maximum bending angle was reached when the electrodes were fully zipped (see Supplementary Methods). We designed a miniaturized and high-performance version of a type of previously reported bending actuator, termed spider-inspired electrohydraulic soft-actuated (SES) joint (*28*), to generate a traveling wave motion in the soft fins. In this design, a stiffening layer introduced an asymmetry in the actuator contraction, resulting in a bending motion (movie S1). We achieved thin millimeter-scale actuators (submillimeter thickness and electrode sizes as low as 27 to 90 mm^2) that operated at voltages (<500 V) far below those typically used for this class of actuators and at a high bandwidth above 100 Hz. These advances were obtained through design, fabrication, and material choices, including the use of a low-viscosity fluorinated fluid as the liquid dielectric and a ferrorelaxor terpolymer as the solid dielectric.

The actuator's downward stroke was electrically driven, whereas the upward motion was due to the release of stored elastic energy. Periodic actuation generated a traveling wave in the soft undulating fin (Fig. 1E). We observed traveling waves for actuation both under water and on the water surface, demonstrating the versatility of this actuation mechanism (Movie 1). Characterizing the traveling wave underwater showed that the wavelength is inversely proportional to the actuation frequency (fig. S1). The combination of robot architecture, locomotion design, and high-performance miniaturized actuators led to high speed and thrust and controlled agile maneuverability. Our tethered and untethered designs achieved both high relative speeds [normalized to a robot's largest dimension, which we define as its characteristic size (CS)] and higher turning speeds compared with other maneuverable bioinspired swimmers (Fig. 1F and table S1).

Performance characterization of tethered modules

The entire locomotion module was monolithically fabricated using a combination of laser processing, lamination, and blade casting (figs. S2 and S3), similar to previously reported methods and materials (*29*). The module consisted of several layers of polyethylene terephthalate (PET), various adhesives, and silicone elastomer (Fig. 2A). For the actuators, we used two different solid dielectrics: a 12-μm-thick PET film with a relative permittivity of 2.2 or a 14-μm-thick layer of the ferrorelaxor terpolymer poly(vinylidene-fluoride–trifluoroethylene–chlorotrifluoroethylene) [P(VDF-TrFE-CTFE)], here referred to as polyvinylidene difluoride–terpolymer (PVDF-terpolymer), with a high relative permittivity (~40) at low frequencies. We used PET as a dielectric because of an easier fabrication process and to explore design rules for the robots; in contrast, we used the PVDF-terpolymer to lower the operating voltage of the actuators to below 500 V to enable untethered operation. We filled the modules with a fluorocarbon liquid (FC 40) because of its low viscosity, which allowed high-frequency actuation. A typical module, with a size of 45 mm by 55 mm by 0.5 mm, where the first dimension is the body length (BL), weighed 1.23 g, lightweight enough to float on the water surface by surface tension.

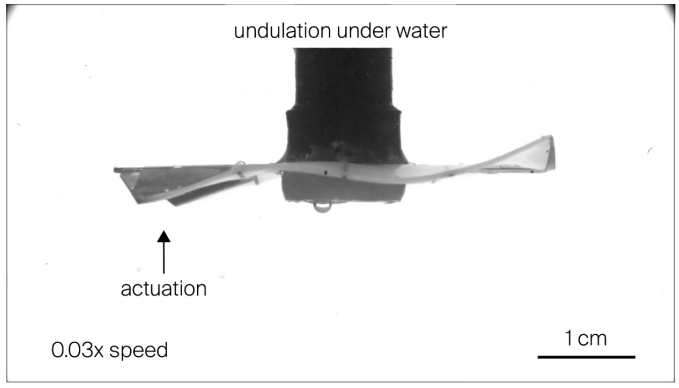

Movie 1. Traveling wave generation in undulating fins. Side view of locomotion modules placed underwater and on the water surface, producing traveling waves in the soft fins. Underwater: A bipolar triangular wave is supplied with an amplitude of 2 kV and at a 16-Hz actuation frequency. Surface: A rectangular wave is supplied with an amplitude of 1.7 kV at a 40-Hz actuation frequency.

We first tested the performance of tethered modules in free-swimming tests, for which we connected the module using thin copper wires (50-μm diameter) in combination with a magnetic connector (Fig. 2B). The modules were driven with a bipolar rectangular voltage signal (typical amplitude is 1700 V; fig. S4) to avoid interfacial charging at the interface of solid and liquid dielectric (*30*). We observed that the swimming speed depended on the actuation frequency and was the highest at 40 Hz, where modules achieved on average a speed of 7.5 ± 0.9 cm/s (1.7 ± 0.2 BL/s), benefiting from resonant behavior (Fig. 2C). The Reynolds numbers for these speeds ranged from 2000 to 5500, indicating a transitional regime between laminar and turbulent flow (see Supplementary Methods).

In tethered modules, the bending stiffness of the thin wires hindered and limited the module's displacement in free-swimming tests, preventing prolonged measurements of swimming speed or lifetime. Rather than the tethered swimming speed, we chose to measure the blocked propulsion force, which is equal to thrust at constant speed. Thrust (T) depends on the square of the swimming speed (v), given by Eq. 1

$$T = c_T \frac{\rho v^2}{2} S \quad (1)$$

where c_T is the thrust coefficient, ρ is the density of water, and S is the wetted surface of the locomotion module (for details, see Supplementary Methods). The surface in contact with water resulted in skin friction drag, given that wave and form drag could be neglected. The wave drag, quantified by the Froude number, was low (<0.12) for our modules, and their cross section perpendicular to the swimming direction was minimal because of the extremely flat design. To measure the thrust, the module was made to swim against

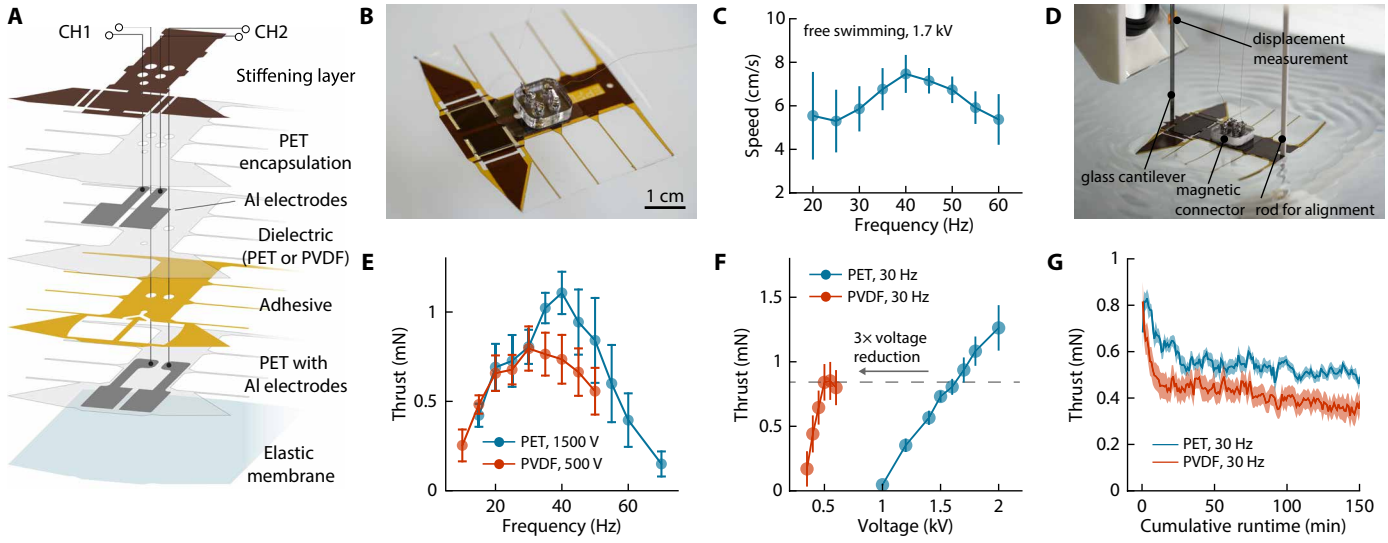

Fig. 2. Performance of tethered soft locomotion modules. (**A**) The locomotion module consists of multiple polymer layers and metal electrodes, enclosing a liquid-filled pouch. (**B**) The module locomotes on the water surface by generating traveling waves. It is connected to an external power supply through thin copper wires and a magnetic connection system, adding 2.25 g to the module. Scale bar, 1 cm. (**C**) Free-swimming tests of modules with a PET dielectric show the highest speed at a 40-Hz actuation frequency. The applied voltage is 1.7 kV. Error bars, standard deviation of the mean for $n = 4$ (for 25- and 30-Hz points) or $n = 3$ (for all other points) samples. (**D**) A measurement of the blocked propulsion force allows controlled characterization of the swimming performance for extended durations. (**E**) The blocked force is maximized at actuation frequencies of 40 and 30 Hz for modules using PET and PVDF-terpolymer as dielectrics, respectively. Error bars, standard deviation of the mean for $n = 5$ samples. (**F**) The blocked force at a fixed frequency of 30 Hz shows a nearly linear trend with applied voltage. Using the PVDF-terpolymer as a dielectric layer enables a threefold reduction in the operating voltage. Error bars, standard deviation of the mean for $n = 4$ (for PET) and $n = 5$ (for PVDF) samples. (**G**) A cumulative run time of more than 2.5 hours is achieved for both dielectrics. With the applied duty cycle of 1:5, the modules were operational for more than 15 hours. Error band, standard deviation of the mean of the data from a 1-min interval.

a glass cantilever, thus avoiding the mechanical influence of the wires (Fig. 2D, fig. S5, and movie S2). The thrust was calculated from the cantilever deflection (see Supplementary Methods). This measurement method was suitable for optimizing driving conditions, varying design parameters, and measuring actuator lifetime in water.

For a drive voltage of 1500 V, we obtained the highest thrust of 1.1 mN (1.6 mN at 1700 V; fig. S6) at a 40-Hz actuation frequency (Fig. 2E). The harmonic oscillation of our actuators was amplified by resonance, and thrust became maximal at the system's natural frequency. When using the PVDF-terpolymer as a dielectric, a thrust of 0.8 mN was reached at a 30-Hz actuation frequency at 500 V. This frequency shift when changing dielectrics stemmed from differences in the thickness of the encapsulation layer in both variants (fig. S2). Using the high-permittivity dielectric, the operating voltages were substantially reduced: Only about one-third of the operating voltage was required when switching from PET to the PVDF-terpolymer, in agreement with our analytic model that predicted a factor of 2.8 (Fig. 2F and Supplementary Methods). The thrust showed a linear dependence on the applied voltage, starting from threshold voltages of about 400 and 1200 V using the PVDF-terpolymer or PET. Typically, both dielectric variants had operating lifetimes of more than 2.5 hours, corresponding to more than 270,000 actuation cycles (Fig. 2G) and more than 750,000 cycles in some cases (fig. S7A). The initial performance remained stable for a few minutes before dropping to 40 to 50% of the initial value. Modules with the PVDF-terpolymer usually showed a faster decrease. This reduction in performance mainly stemmed from mechanical fatigue of the actuator pouches, given that electrical breakdowns played a minor role (fig. S7, B and C). When using thin metal electrodes (~50 nm) and moderate voltages, electrical breakdowns led to ablation of the electrodes in the region of failure without damaging the shell material. This self-clearing effect let the actuators withstand several breakdown events with a minimal effect on the actuator's performance.

Scaling analysis

Using thrust as a performance metric enabled us to compare various robot designs (an overview is given in fig. S8). We performed a scaling analysis, both experimentally and analytically, of two major design parameters: scaling of the fin span (or width of the fin) of the module at constant body length and scaling of the module's width and length at a constant aspect ratio. We modeled the actuators as driven harmonic oscillators with spring constant k and damping coefficient γ to understand the behavior of frequency and thrust under such scaling conditions. For the first scenario, we kept both the body length (45 mm) and the size of the actuators constant but scaled the span of each fin from 10 to 30 mm (Fig. 3, A and B). The size of the fin had a threefold effect on swimming performance:

First, we found that the optimal actuation frequency (f_{opt}), which maximizes thrust and equals the systems' natural frequency, scales inversely with the span (W) and is given by Eq. 2

$$f_{opt} = \frac{1}{2\pi}\sqrt{\frac{k}{\varsigma W^2}} \quad (2)$$

This was a direct consequence of the added mass from larger fins and from the mass of water that was moved with this oscillation (see Supplementary Methods for details). The total oscillating mass is related to the square of the fin span through the coefficient ς with the unit kg/m^2.

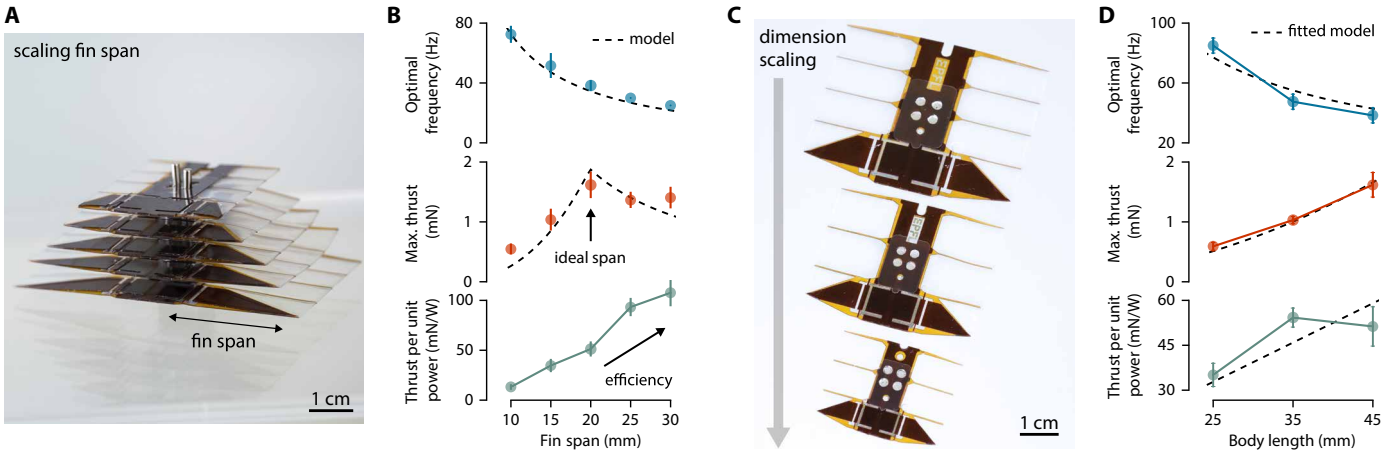

Fig. 3. Scaling analysis of tethered soft locomotion modules. (**A**) Modules with a scaled fin span but equally dimensioned actuators and body length. Scale bar, 1 cm. (**B**) Modules with a larger fin span operate best at lower actuation frequencies, deliver a high thrust, and hence show increased swimming efficiency. Dashed lines are analytic models quantifying the frequency behavior and indicating an ideal fin span. Error bars, standard deviation of the mean for $n = 3$ (for 15- and 20-mm fin spans), $n = 4$ (for 10- and 30-mm fin spans), and $n = 6$ (for 25-mm fin span) samples. (**C**) Modules with constant aspect ratio and scaled body lengths of 45, 35, and 25 mm. Scale bar, 1 cm. (**D**) Larger modules have lower optimal actuation frequencies and achieve a higher maximal thrust. The swimming efficiency is higher for larger modules. Dashed lines are least square regressions of the data using the derived scaling laws (inverse power law for optimal frequency, quadratic power law for maximum thrust, or linear law for thrust per unit power). Error bars, standard deviation of the mean for $n = 4$ (for 25- and 35-mm body lengths) and $n = 3$ (for 45-mm body length) samples. Error bars for the measurement of optimal frequency, systematic error corresponding to the chosen frequency interval (5 Hz).

Second, the fin span led to limits on amplitude because of energy conversion and range of motion limits. We measured maximal thrust at a span of around 20 mm. This optimal fin span (W_{opt}) resulted from the conversion of a fixed electrical input energy, limited by the applied voltage, to mechanical output energy, with efficiency η. The actuators' maximum bending angle (α_{max}) also limited mechanical output energy. The optimal span was found at the intersection of the energy conversion and range of motion limits (fig. S9). For a fixed input voltage (U) and the effective capacitance of an actuator (C), the optimal span is given by Eq. 3 (see Supplementary Methods for details)

$$W_{opt} = \sqrt{\frac{U}{\sin \alpha_{max}} \frac{\gamma}{k} \sqrt{\frac{\eta C}{\varsigma}}} \quad (3)$$

The optimal span depended only implicitly on the length of the robot through the magnitude of the spring constant and the damping coefficient, which we determined experimentally (fig. S9A).

Third, the size of the fin span affected swimming efficiency. The ratio of thrust to input electrical power, a quantity that relates to swimming efficiency, increased with larger spans. For capacitive actuators, the power consumption was found to be directly proportional to their actuation frequency and capacitance in the fully actuated state (fig. S10). The largest module with a fin span of 30 mm, for example, achieved its highest thrust (1.4 mN) at 25 Hz, consuming 13 mW. Under driving conditions that maximize thrust, the lowest cost of transport (COT) was 14 for a 30-mm fin span (fig. S11A). Notably, the minimal COT was achieved at frequencies that are lower than the optimal frequency. For a module with a span of 20 mm, we measured its minimal COT of 13 in the range of 15 to 20 Hz (fig. S11B). Applications that do not require high speed or thrust can benefit from the more energy-efficient locomotion at lower actuation frequencies.

Similar trends were observed when uniformly scaling the robot's width and length. We investigated three module sizes measuring 45, 35, and 25 mm in length and observed that the optimal actuation frequency increased for smaller modules as the thrust decreased (Fig. 3, C and D, and fig. S6). These trends are in line with an analysis of two-dimensional scaling, where the optimal frequency scaled inversely with size and the thrust scaled with the square of size. The thrust per unit power increased linearly with size, making larger modules more energy efficient. Experimentally, the similar performance for 35 mm– and 45 mm–sized modules likely stemmed from slight variations in the used encapsulation layers, given that a thicker encapsulation was used in the 45-mm module.

In this work, we focused on designs and driving conditions that maximize speed and thrust rather than energy efficiency. To this end, modules with a 45-mm length and a 20-mm fin span represented the optimal configuration for the untethered robots.

Swimming mechanisms and maneuverability

Our robot swam and steered using a pair of undulating pectoral fins (Fig. 4A). Although this propulsion mechanism is commonly found for animals underwater, it is rarely used—if at all—by animals moving on the water surface. The relation discussed above between actuation frequency and swimming speeds and thrust allowed finding optimal driving parameters. Here, we visualized the generated surface flow using line integral convolution (LIC) and particle image velocimetry (PIV) to get insights into the mechanisms of propulsion (Fig. 4, B and C, and movie S3). For forward propulsion, both fins pushed flow to the side and the back to generate counterrotating recirculation regions behind the robot, which produced a thrust wake pushing the module forward (Fig. 4B). Similar patterns that generate thrust are observed for water striders and honey bees swimming at the air-water interface (*31*, *32*). The velocity of the backward flow (relative to the module) and the width of the recirculation region had a frequency behavior similar to that of the module's swimming

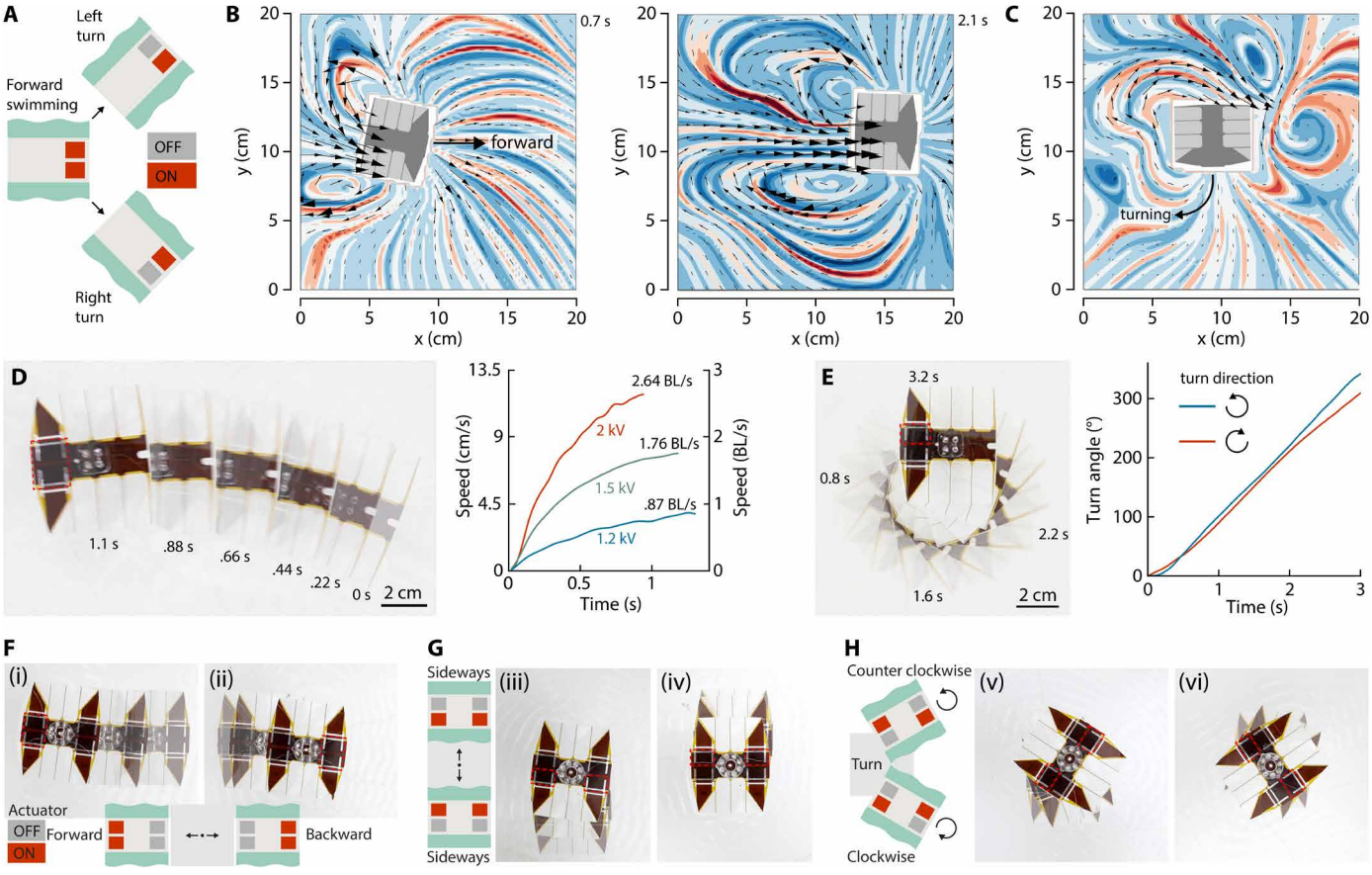

Fig. 4. Versatile maneuverability through two- and four-actuator designs. (**A**) Control scheme for a two-actuator locomotion module. Forward swimming is achieved by applying voltage to both actuators, whereas rotation is achieved by using a single actuator. (**B** and **C**) Flow visualizations using LIC show (B) two counterrotating recirculation regions symmetrically located behind the locomotion module that yield forward propulsion and (C) an asymmetric wake pattern when the robot is turning. Black arrows show the surface velocity field. (**D** and **E**) Swimming and rotation speed for the best-performing tethered locomotion module. (D) The locomotion module reaches up to 2.6 BL/s (12 cm/s) for forward motion and (E) 120°/s for turning for both directions. Scale bar, 2 cm. (**F** to **H**) A four-actuator design increases functionality by adding backward (ii) and sideways (iii and iv) motion to forward (i) and turning (v and vi) motions. The module can seamlessly switch between (F) forward (6.7 cm/s) and backward (6.4 cm/s) motion by using the front or rear pair of actuators. (G) Sideways locomotion is enabled by using either left or right actuators, resulting in directional locomotion at reduced speed (2.8 and 4.1 cm/s). (H) Rotations are achieved by using either a single actuator or a diagonal pair of actuators. Scale bar, 2 cm.

speed. The backward flow was maximized and the width of the recirculation region was minimized at 40 Hz, correlating performance to the generation of surface flows (fig. S12). If only one single fin is driven, the recirculation region became asymmetric and resulted in the rotation of the robot (Fig. 4C). In addition to the surface flows, the locomotion module generated rearward jets underwater, which we qualitatively visualized in movie S4 for propulsion on the surface and in fig. S13 for underwater operation. Propulsion was caused by a combination of surface and underwater flows, similar to the hydrodynamics observed in other small-scale swimmers (*25*, *32*). Investigating the relative contributions of these flows will be part of future studies.

For forward propulsion, the fastest module accelerated to 12 cm/s (2.6 BL/s) within a few seconds, with a peak acceleration of 38 cm/s^2 at 2 kV (Fig. 4D). In some cases, we observed that the locomotion module deviated from a perfectly straight path because of small differences in the fabrication of right and left actuators. Tuning the actuation frequency of each fin individually, using a closed-loop control, would allow swimming along complex trajectories. The undulating fin design and fast acceleration led to high agility. Locomotion modules turned almost on the spot (turning radius as small as 20 mm) with an angular speed of ~120°/s at 1.7 kV (Fig. 4E and movie S5).

In a slightly different embodiment of the robot, the locomotion capabilities were further enhanced by adding two additional actuators on the rear side of the robot, mirroring the module at its central axis. Depending on the active pair of actuators, the module swam forward, backward, or sideways or turned, rendering a vehicle similar to quadcopter drones but for the water surface (Fig. 4, F to H, and movie S6). Notably, this four-actuator module reached similar speeds for both forward (6.7 cm/s at 1.7 kV) and backward (6.4 cm/s) locomotion, comparable to two-actuator modules (fig. S14). Sideways locomotion was achieved when two actuators of the same side were activated, resulting in speeds up to 4 cm/s. Turning was achieved by using either a single actuator or a pair of actuators along the diagonal. In the latter case, the module turned with an angular speed up to 95°/s. These results demonstrate that with a limited number of actuators, a full range of maneuvers is achieved,

enabling the propulsion needed for sophisticated operation scenarios on cluttered water surfaces.

Autonomous untethered swimming robots

Operation in most natural environments requires the robot to be untethered. To this end, we developed a small PCB that includes all elements needed to operate autonomously (Fig. 5A). A key element in the PCB is a multichannel HVPS that provided two individually controlled channels of bipolar voltage signals at more than 500 V, driving the two actuators using the PVDF-terpolymer as the solid dielectric (Fig. 5B). In addition to the HVPS, the PCB hosted a microcontroller (MCU) and sensors for remote control and autonomous operation (fig. S15). To generate a high-voltage output, the HVPS amplified the input from a lithium-ion battery (~3.7 V) to more than 500 V using an open-loop flyback converter circuitry (FBC) (*33*). The magnitude of the output voltage was mainly influenced by the pulse width and frequency of the MCU's control signal (Fig. 5C). Aiming for an output voltage higher than 500 V, we found that a frequency of 20 kHz with a pulse width of 2.5 μs was a practical compromise between output voltage and power consumption (about 500 to 600 mW; see Supplementary Methods). The high voltage was supplied to the actuators via two individually controlled full bridges, which switched the output, including its polarity, to charge and discharge the actuators. The voltage delivered to the actuators depended on how many

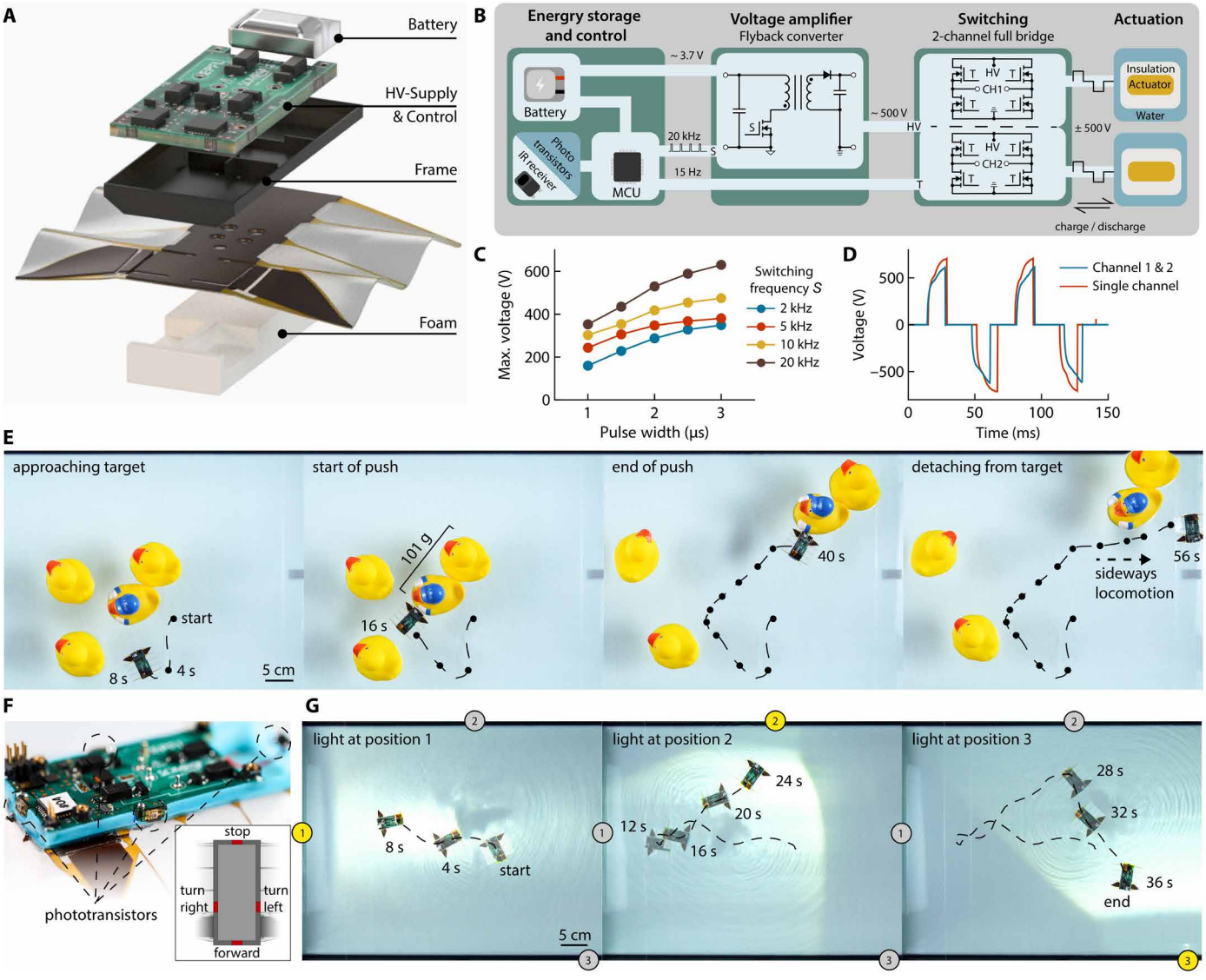

Fig. 5. Untethered remote-controlled and autonomous swimming robots. (**A**) Exploded schematic view of the untethered robot. (**B**) Simplified block diagram of the high-voltage (HV) power supply, control components, and their connections to the actuators. (**C**) Maximal output voltage of the flyback converter as a function of the control signal, which is supplied to switch *S* on the primary side of the transformer. (**D**) Voltage measured at the input of the actuators as a function of time and for forward control (channels 1 and 2) and rotation (single channel) using a switching frequency of 20 kHz with a pulse width of 2.5 μs. (**E**) Remote-controlled robot approaching, pushing away, and detaching from obstacles that are 16 times heavier than the robot itself. Points on the trajectory indicate the robot's position in 4-s intervals. Scale bar, 5 cm. (**F**) Autonomous robot equipped with four phototransistors to detect the direction of an external light source. (**G**) Autonomous robot swimming in the direction of external sources of white light, which are activated in sequence. Scale bar, 5 cm.

actuators are active and what actuation frequency was used (Fig. 5D and fig. S15). For the 30-Hz actuation frequency, the HVPS supplied up to 710 V to a single actuator and 620 V if both actuators were addressed. Although the output power of the HVPS was sufficient to drive the actuators in their optimal configuration, power limitations were visible in the rise time needed to reach maximum voltage, which was a compromise when choosing smaller electrical components.

We first steered the robot using a four-button remote control based on infrared communication. An infrared receiver on the robot's PCB decoded the control signals and sent them to the MCU, which controlled the HVPS and the high-voltage switches. We mounted the PCB with the battery in a 3D-printed tray, which protected the electronics from water, and mechanically connected it to the locomotion module. Because the added weight (~5 g) of the PCB, battery, and tray exceeded the weight-bearing limit of the locomotion module (fig. S16), we added a thin foam layer under the locomotion module to increase buoyancy, resulting in a total weight of the robot of 6.23 g.

The untethered robot swam forward with up to 5.14 cm/s (1.14 BL/s) and made turns to both the left and right with up to 195°/s (fig. S17). Given its speed, robustness, and maneuverability, the robot was capable of swimming through narrow spaces (Movie 2, and movie S7) and pushing away obstacles (movie S8). We showed that the robot can displace obstacles weighing 16 times (101 g) its own body weight (Fig. 5E and movie S8). Once engaged with a targeted obstacle, a series of turning movements led to the detachment of the robot from the obstacle and to the continuation of its task.

To go from remote-controlled operation to autonomous operation, we installed four phototransistors around the robot (Fig. 5F). The robot compared the measured light intensities and was programmed to swim toward the direction of highest intensity. This added autonomy enabled the robot to follow a moving light source or to swim toward various light sources guiding a task (Fig. 5G and movies S9 and S10).

DISCUSSION

We demonstrated here a centimeter-scale, untethered, and autonomous swimming robot with high speed, thrust, and agility. The flat, monolithically fabricated locomotion module allowed robust propulsion on the water surface and thus enabled practical applications in cluttered environments. By the effective use of undulating fin propulsion, our robots were capable of rapid turns (up to 195°/s) with small turning radii (20 mm) and of swimming forward, backward, and sideways. Modeling the actuator amplitudes as a function of frequency allowed us to derive design guidelines to optimize speed and thrust for a given robot size. We provide a scaling analysis to quantify compromises between size, performance, and efficiency. These considerations led to an untethered robot carrying a miniature power supply, control electronics, and sensors. The undulating fins generated thrust in the millinewton range, allowing the robot to move objects weighing 16 times the robot's mass. The integrated sensors enabled the robot to autonomously navigate, locate, and home toward light sources. We achieved these capabilities through the frugal yet effective use of high-performance electrohydraulic actuators to enable undulatory propulsion with high thrust.

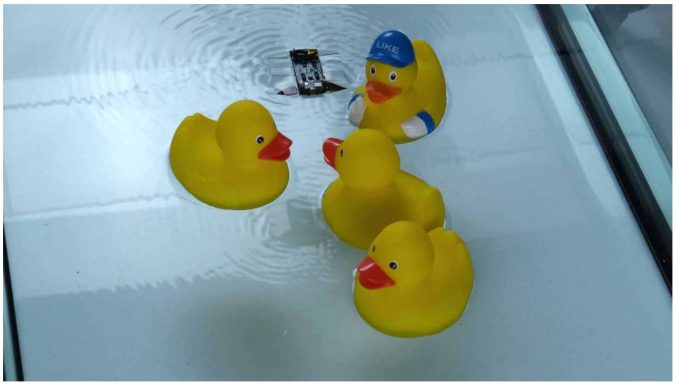

Movie 2. Swimming through floating objects. An untethered, remote-controlled robot is steered through a set of floating objects. The gaps between objects are narrow, measuring about the size of the robot.

We chose to optimize driving conditions and fin dimensions to maximize thrust to enable rapid maneuvers or to move floating obstacles. Naturally, these high-thrust driving conditions came at the cost of reduced energy efficiency and, hence, of reduced battery lifetime. Extended outdoor operations would benefit from driving conditions that optimize energy efficiency rather than thrust. The power consumption of electrohydraulic actuators decreases when driven at lower frequencies. Optimizing the resonant behavior of actuators, by tuning the robot's size or the mechanical properties of its body, presents a path to enable swimming with high efficiency. Increasing the actuator's range of motion, by achieving larger bending angles, would allow for large oscillation amplitudes, higher speeds, and lower COT. For the type of actuator that we used, bending angles up to 70° have been demonstrated (*28*). However, such deformations require much larger driving voltages, which are impractical for many untethered applications, given that this would increase the weight and size of the driving electronics by an order of magnitude.

For the untethered robots, because of the used HVPS architecture, power consumption was dominated by the high-voltage generation. When the robot was resting, the entire electronics, including computing, sensing, and high-voltage generation, required 530 mW. When both actuators were driven at 30 Hz, the power consumption increased by only about 10%. Strategies to achieve higher system efficiencies must target the HVPS design. Solutions for highly efficient voltage amplification, with more than 90% efficiency, already exist (*34*). However, they are not commercially available and are work intensive to integrate in a customized PCB. Translating current academic efforts toward commercial products will immensely boost the potential of robots driven by electrostatic actuators.

Applications of surface-swimming robots, such as exploring or wildlife imaging, require longer total run times. Now, the 30-mAh onboard battery was sufficient to drive the robot for about 10 min. Including energy harvesting through a solar cell on top of the robot would allow to increase the operational time by recharging the battery when the robot is at rest. Monocrystalline Si-based solar cells, of the same size as our robots, are commercially available and weigh about 1 g, increasing the robot's weight by 15%. Ultralightweight photovoltaic modules, used to recharge quadcopter drones (*35*), deliver 44 W g^{-1} and will enable recharging without affecting the payload of the robot.

Beyond energy autonomy, many applications would benefit from a higher degree of decision autonomy. Although we demonstrated basic navigation autonomy through an array of light sensors, more

advanced sensing will increase the intelligence of the robot. The PCB with a microcontroller allows readily incorporating a wide range of sensors and communication systems (such as Bluetooth modules or optical) adapted to specific tasks. Chemical sensors for monitoring water quality, cameras for mapping and exploring unknown environments, and hydrophones and sonars are examples of sensors that would augment the capabilities of a surface-swimming robot. The shape and design of our robot allow facile integration of components on commercial PCBs while providing stable locomotion. Trade-offs exist for the size of electrical components, the robot's size, and its energy requirements. When small scales become important, collective intelligence in robotic swarms becomes a promising avenue. Manufacturing robots at large quantities benefits from the low-cost materials and fabrication methods developed in this study. Strategies that enable communication directly between robots are needed for swarm behavior.

Last, using small-scale robots underwater has potential in the exploration of complex underwater environments such as coral reefs. Although we demonstrated traveling wave generation underwater, the current robot design needs to be improved to allow for autonomous locomotion underwater. Buoyancy needs to be actively controlled using an additional actuator or gas generators (for example, through hydrolysis). Because the actuator's upward stroke is driven by mechanical relaxation, the actuation frequency is limited by the time constant of this process. On the water surface, this relaxation is aided by energy stored in the deformation of the water surface, but underwater, the relaxation step is slower. Using antagonistic pairs of actuators to drive both downward and upward strokes would allow more effective propulsion underwater. The robots presented here will drive further research on miniature robots for aquatic environments and pave the way for the next generation of aquatic drones that support applications in exploring bodies of water, aquatic biology, aquafarming, and agriculture.

MATERIALS AND METHODS

Comparison of swimming robots

In our comparison of swimming robots, we were using average speeds for linear motion and rotation. The speed was averaged over at least two actuation cycles. Motion tracking using Kinovea software was used if no values but videos were available in the literature. We normalized the speed with respect to the robot's CS, which is its largest dimension. This approach gives a better comparison between robot designs with different aspect ratios.

Fabrication of locomotion modules

Fabrication of robots with a PET dielectric

Mylar (a type of biaxially oriented PET, 12 μm thick) metalized with 30-nm aluminum (ES301913, GoodFellow) was used for the electrode layer. An etching mask was printed onto the metalized film using a solid ink printer (Xerox ColorQube 8580), and the electrodes were etched using a 2% weight potassium hydroxide solution at room temperature. The etch mask was then transferred from the Mylar to regular printing paper using a laminator (Matrix Duo MD-460, Vivid) at 120°C. The electrode layers were then laser cut (Speedy 300, Trotec). A thermal adhesive (Thermal Bonding Film 583, 3M) was cut and laminated first onto the bottom electrode layer (with the electrode facing the adhesive) at 120°C and then onto the Mylar side of the top electrode layer at 135°C, resulting in a Mylar-Al-Mylar-Al structure. We added a sealing layer onto the top electrode to prevent contact with water. For this layer, we cast a 10-μm-thick layer of thermal adhesive (Vitel 3350B from Bostik, dissolved in methyl ethyl ketone) onto 25-μm-thick Mylar, structured it using laser cutting, and laminated it onto the top electrodes at 120°C. For modules with 35-mm and 25-mm BLs, we used a 10-μm-thick layer of polystyrene (Sigma-Aldrich) as encapsulation instead of PET. A stiffening layer was cut from 250-μm-thick PET (McMaster) and fixed onto the top side of the layer structure with a double-sided adhesive (50-μm-thick, ARcare, Adhesives Research). The assembly was again structured using a laser cutter to define the soft fins. We cast a layer of Ecoflex-30 (Smooth-On) on the bottom side of the assembly and cured it at 65°C for 4 hours. Before the elastomer was cast, the bottom side of the assembly was activated with oxygen plasma (70 W, 3 min, Diener Atto) to increase adhesion. We laser cut the robot again to define its final shape. The dielectric liquid (Fluorinert FC-40, 3M) was injected under a constant pressure of 30 mbar through a filling hole and sealed using the double-sided tape and a 25-μm-thick layer of Mylar. For all locomotion modules, we used a single port to fill multiple actuators. This port was sealed after filling but left a small channel that connected all actuators, even during operation. We found that this method was a frugal way to equally distribute the liquid in the pouches, to maintain equal filling pressures, and to obtain similar performance of all actuators on the module. A typical locomotion module with a 45-mm BL had 55 ± 5 μl of dielectric liquid filled into both actuators.

Fabrication of robots with a PVDF dielectric

For locomotion modules with PVDF-terpolymer as a dielectric, the same steps were applied for fabricating the electrodes as described above. A 14% weight solution of P(VDF-TrFE-CTFE) (Piezotech RT-TS, Arkema) in methyl ethyl ketone was cast on the top electrode layer using a thin film applicator (Zehntner ZAA 2300) with a gap of 288 μm, resulting in a roughly 14-μm-thick layer of P(VDF-TrFE-CTFE). During the casting process, we used a mask (GP20, Nexus, 80 μm) to pattern the dielectric around the electrodes only. The top electrode layer with a PVDF dielectric was annealed for 1 hour at 105°C. The bottom and top electrode layers were laminated at a maximum temperature of 120°C, resulting in a Mylar-Al-PVDF-Al-Mylar structure. Given that the top electrode was already isolated from water through its Mylar substrate, an additional sealing layer was omitted in this design. The fabrication further followed the steps as described above. During the assembly of bottom and top electrodes, a conductive silicone-based adhesive (SS-27, Silicone Solutions) was applied on the rear side of the locomotion module to have the contact pads of the top electrode facing upward.

Characterization of locomotion modules

Traveling wave underwater

We produced a traveling wave underwater (Fig. 1E and Movie 1) supplying a bipolar triangular high-voltage signal with an amplitude of 2 kV. The actuation frequency of the 45-mm-long module was 16 Hz. The sequence was filmed using a high-speed camera (Phantom VEO310L).

Free-swimming measurements

Locomotion modules with a PET dielectric were positioned on the water surface and connected with a magnetic connector (2.25 g) and two copper wires (50-μm diameters) to an external power supply (Trek 609E-6). We supplied a bipolar rectangular signal at various frequencies and voltages to drive the robot (fig. S3). The swimming

speed was determined by filming the robot from the top and image tracking using Kinovea software.

Blocked force measurements

The robots were positioned in front of a hollow glass cantilever (0.05 mm by 1.00 mm, Hollow Rectangle Capillaries, CM Scientific) and on the water surface of a tank measuring 30 cm by 20 cm by 20 cm (halfway filled). Each robot was connected with the magnetic connector and two copper wires (50-μm diameters) to an external power supply (Trek 609E-6). We supplied a bipolar rectangular signal at various frequencies and voltages to drive the robot. The deflection of the cantilever was measured with a laser displacement sensor (IL-065, Keyence) and recalculated into a force value (see Supplementary Methods). The robot was activated for 5 s for each driving parameter, and the mean blocked force was determined between 2.5 and 5 s after the robot started to swim.

Load carrying measurements

Locomotion modules with a PET dielectric were placed into the setup for measuring the blocked force and sequentially loaded with evenly distributed weights. Robots were tested at 40 Hz and at 1.5 and 1.7 kV.

Lifetime measurements

The locomotion modules were placed into the setup for measuring the blocked force. We tested modules with a PET dielectric at 30 Hz and supplying 1500 V and modules with a PVDF-terpolymer dielectric at 30 Hz and 500 V. For both designs, we let the robots continuously swim for 5 min followed by a 10-min break. We repeated this cycle until the failure of the modules. Data are averaged from a 1-min interval.

Actuator power consumption

The power consumption was measured using the voltage and current monitor of the Trek high-voltage amplifier. Each measurement was calibrated by measuring the power consumption when no load (locomotion module) was connected to the power supply.

Estimation of oscillator parameters of actuators

We estimated the spring constant and damping coefficient of our actuators experimentally. To this end, we measured the frequency behavior of an actuator in air and without a soft fin (fig. S9a). This had the advantage that there was no influence of water or fin, and the oscillating mass ($m_{air} = 0.1$ g) was known. Fitting the response function to the measurement in air resulted in $k = 0.94$ N/m and $\gamma = 0.018$ kg/s, and the resonance frequency was 49 Hz.

Traveling wave metric and underwater PIV measurements

Locomotion modules were connected with a stiff, 3D-printed connector to a custom-made power supply. The modules were placed underwater and filmed from the side using a high-speed camera (Photron SA-X2 with Canon EF 100 mm f/2.0 lens) at an image acquisition rate of 500 to 1000 Hz depending on the actuation frequency of the locomotion module. A light sheet generated with a high-power light-emitting diode (LED) (ILA_5150, LED Pulsed Systems) was used to illuminate the edge of the module's fin. We supplied a bipolar rectangular voltage signal (1500-V amplitude) and recorded the fin profiles for various frequencies.

Water was seeded with 56-μm polyamide particles (VESTOSINT). The flow around the robot was imaged with the high-speed camera at 125 Hz. The imaging plane was illuminated using the high-power LEDs in continuous mode. The n and $n + 10$ particle images were correlated using a multigrid evaluation method with a final window size of 48 pixels by 48 pixels and a step size of 16 pixels, or 66% overlap, resulting in a physical resolution of 2.07 mm.

LIC and surface PIV measurements

Locomotion modules (PET dielectric) were placed on the water surface of a tank measuring 30 cm by 30 cm by 60 cm and filled halfway. Particles from milled black pepper were added to the water surface. An LED panel with a light diffuser was placed below the water tank to provide continuous back-illumination of the particles. A high-speed camera (Photron SA-X2 with Canon EF 100 mm f/2.0 lens) recorded the surface motion from above. Recording was manually started and stopped to capture the full motion of the robot, including the acceleration and deceleration phases. The modules were driven by a custom-made multichannel power supply, typically supplying a bipolar rectangular signal of 1.7 kV and at various frequencies.

Images were acquired at 250 and 500 Hz by the high-speed camera with a definition of 1024 pixels by 1024 pixels. Particle images were correlated using a multigrid evaluation method with a final window size of 96 pixels by 96 pixels and a step size of 10 pixels (overlap of 90%), resulting in a physical resolution of 2.04 mm.

The position and orientation of a module were obtained for each frame by finding the maximum cross-correlation of the image and the module's outline. A rectangle was used to mask the module during PIV processing. The signals in the masked regions were not correlated during PIV processing.

LIC figures indicated the flow topology by filtering color patterns along local streamlines (*36*). Two convolution passes were applied to pink noise patterns with a normalized standard deviation of 0.15.

Characterization and assembly of an untethered robot

Measurement of HVPS output voltage

The PCB was connected to two external power supplies (Aim-TTI EL302, maximum current of 2 A) to find an ideal configuration, resulting in a high FBC output voltage and reasonable power consumption. The first one, set to 3.9 V, replaced the battery, whereas the second one, set to 3.3 V, powered the control circuit of the PCB. We varied the pulse width of the signal used to control the switch on the primary side of the FBC (within the range from 1 to 3 μs) and the frequency of this signal (within the range from 1 to 20 kHz). Voltage output was measured in four configurations: first, at the output of the FBC with none of the full bridges active; second, at the output of channel 1 (CH1) with only the first full bridge active; third, at the output of channel 2 (CH2) with only the second full bridge active; and fourth, at both CH1 and CH2 with both full bridges active. Output voltages were measured using a high-voltage probe (GW Instek GDP-050) and an oscilloscope (Analog Discovery Pro ADP3450).

Measurement of power consumption

For measuring the power consumption, the FBC was either off or driven under the constant conditions of a 2.5-μs pulse width at 20 kHz and a 15-Hz full bridge switching frequency, which resulted in a 30-Hz actuation frequency. The entire PCB was powered by a lithium-ion battery. A 1-ohm resistance was inserted between the negative side of the battery and the PCB to measure the current and calculate the power consumption. Simultaneously, the output voltage of the FBC was measured as described above.

Untethered robot

For the assembly of untethered robots, we chose locomotion modules with a 45-mm length and a 55-mm width and with PVDF-terpolymer as a dielectric. Plastic trays were 3D printed (aqua hyperfine resin, Phrozen) and postprocessed by laser machining. First, the PCB (designed in Altium Designer, produced by Eurocircuits; components are listed in table S2) and the tray were assembled. To this end,

6.9-mm-long pins (nail head pin, Mill-Max), serving as connections to the locomotion module, were guided from the bottom side through both the tray and PCB and soldered from the top. Moisture curing conductive silicone (SS-27, Silicone Solutions) was applied to the connection pins to establish contact to the locomotion module. Thin lines of silicone sealant (Sil-poxy, Smooth-On) were applied on the locomotion module, and the tray and PCB were placed on top of the module. Sealants and conductive silicone were cured for a minimum of 4 hours at room temperature. Two layers of polystyrene foam (each 3 mm thick) were cut and glued on the bottom side of the robot using ultraviolet-curable glue (Bluefixx repair). A lithium-ion battery with a nominal capacity of 30 mAh and a manual on/off switch were mounted on the PCB, finalizing the robot. For the autonomous version of the robot, we soldered four phototransistors on each side of the robot.

Characterization of the untethered robot

If not mentioned otherwise, untethered robots were operated in a tank with dimensions of 130 cm by 50 cm by 50 cm. The fill level of water was about 15 cm. A cluttered environment, simulating a rice field, was set up in a small inflatable swimming pool using cat grass as plants. Except for the autonomous robot, robots were remote controlled using the aforementioned infrared controller. For the autonomous robot, we used various commercial white light sources, which were manually controlled. Swimming speed and trajectories were taken from image analysis using Kinovea software.

Statistical analysis

Figures present data from individual experiments without the application of statistical methods, unless noted otherwise. All data are reported as either the means or the means ± standard deviation, unless specified differently. The number of samples is given in the figure captions.

Supplementary Materials

The PDF file includes:
Methods
Figs. S1 to S17
Tables S1 and S2
Legends for movies S1 to S10
References (*37*–*47*)

Other Supplementary Material for this manuscript includes the following:
Movies S1 to S10

REFERENCES AND NOTES

1. M. Dunbabin, L. Marques, Robots for environmental monitoring: Significant advancements and applications. *IEEE Robot. Autom. Mag.* **19**, 24–39 (2012).
2. R. K. Katzschmann, J. DelPreto, R. MacCurdy, D. Rus, Exploration of underwater life with an acoustically controlled soft robotic fish. *Sci. Robot.* **3**, eaar3449 (2018).
3. G. Li, X. Chen, F. Zhou, Y. Liang, Y. Xiao, X. Cao, Z. Zhang, M. Zhang, B. Wu, S. Yin, Y. Xu, H. Fan, Z. Chen, W. Song, W. Yang, B. Pan, J. Hou, W. Zou, S. He, X. Yang, G. Mao, Z. Jia, H. Zhou, T. Li, S. Qu, Z. Xu, Z. Huang, Y. Luo, T. Xie, J. Gu, S. Zhu, W. Yang, Self-powered soft robot in the Mariana Trench. *Nature* **591**, 66–71 (2021).
4. T. Wang, H.-J. Joo, S. Song, W. Hu, C. Keplinger, M. Sitti, A versatile jellyfish-like robotic platform for effective underwater propulsion and manipulation. *Sci. Adv.* **9**, eadg0292 (2023).
5. C. Alt, M. Moerdijk, K. Lehleiter, N. Peltzer, T. Trapp, M. Purucker, J. Spohrer, C. Trapp, P. Steck, P. Ruegg, BionicFinWave: Underwater robot with unique fin drive (Festo, 2019); https://www.festo.com/us/en/e/about-festo/research-and-development/bionic-learning-network/highlights-from-2015-to-2017/bionicfinwave-id_32779/.
6. M. Sfakiotakis, R. Gliva, M. Mountoufaris, Steering-plane motion control for an underwater robot with a pair of undulatory fin propulsors, in *2016 24th Mediterranean Conference on Control and Automation (MED)* (IEEE, 2016), pp. 496–503.
7. L. Liu, Y. Li, Y. Wang, X. Ma, Design and preliminary evaluation of a biomimetic underwater robot with undulating fin propulsion. *IOP Conf. Ser. Mater. Sci. Eng.* **790**, 012160 (2020).
8. Y. Chen, N. Doshi, B. Goldberg, H. Wang, R. J. Wood, Controllable water surface to underwater transition through electrowetting in a hybrid terrestrial-aquatic microrobot. *Nat. Commun.* **9**, 2495 (2018).
9. Y. S. Song, M. Sitti, Surface-tension-driven biologically inspired water strider robots: Theory and experiments. *IEEE Trans. Robot.* **23**, 578–589 (2007).
10. Y. S. Song, M. Sitti, STRIDE: A highly maneuverable and non-tethered water strider robot, in *Proceedings 2007 IEEE International Conference on Robotics and Automation* (IEEE, 2007), pp. 980–984.
11. Y. Du, B. Peng, W. Zhou, Y. Wu, A piezoelectric water skating microrobot steers through ripple interference, in *2022 IEEE 35th International Conference on Micro Electro Mechanical Systems Conference (MEMS)* (IEEE, 2022), pp. 644–647.
12. B. Kwak, S. Choi, J. Maeng, J. Bae, Marangoni effect inspired robotic self-propulsion over a water surface using a flow-imbibition-powered microfluidic pump. *Sci. Rep.* **11**, 17469 (2021).
13. J.-W. Mao, D.-D. Han, H. Zhou, H.-B. Sun, Y.-L. Zhang, Bioinspired superhydrophobic swimming robots with embedded microfluidic networks and photothermal switch for controllable *Marangoni* propulsion. *Adv. Funct. Mater.* **33**, 2208677 (2023).
14. J. Ko, C. Kim, D. Kim, Y. Song, S. Lee, B. Yeom, J. Huh, S. Han, D. Kang, J.-S. Koh, J. Cho, High-performance electrified hydrogel actuators based on wrinkled nanomembrane electrodes for untethered insect-scale soft aquabots. *Sci. Robot.* **7**, eabo6463 (2022).
15. S. Wang, B. Huang, D. McCoul, M. Li, L. Mu, J. Zhao, A soft breaststroke-inspired swimming robot actuated by dielectric elastomers. *Smart Mater. Struct.* **28**, 045006 (2019).
16. B. Kwak, J. Bae, Toward fast and efficient mobility in aquatic environment: A robot with compliant swimming appendages inspired by a water beetle. *J. Bionic Eng.* **14**, 260–271 (2017).
17. G. Mao, D. Schiller, D. Danninger, B. Hailegnaw, F. Hartmann, T. Stockinger, M. Drack, N. Arnold, M. Kaltenbrunner, Ultrafast small-scale soft electromagnetic robots. *Nat. Commun.* **13**, 4456 (2022).
18. E. Rhee, R. Hunt, S. J. Thomson, D. M. Harris, SurferBot: A wave-propelled aquatic vibrobot. *Bioinspir. Biomim.* **17**, 055001 (2022).
19. D. Wang, Y. Liu, J. Deng, S. Zhang, J. Li, W. Wang, J. Liu, W. Chen, Q. Quan, G. Liu, H. Xie, J. Zhao, Miniature amphibious robot actuated by rigid-flexible hybrid vibration modules. *Adv. Sci.* **9**, 2203054 (2022).
20. T. Li, G. Li, Y. Liang, T. Cheng, J. Dai, X. Yang, B. Liu, Z. Zeng, Z. Huang, Y. Luo, T. Xie, W. Yang, Fast-moving soft electronic fish. *Sci. Adv.* **3**, e1602045 (2017).
21. Y. Chi, Y. Hong, Y. Zhao, Y. Li, J. Yin, Snapping for high-speed and high-efficient butterfly stroke–like soft swimmer. *Sci. Adv.* **8**, eadd3788 (2022).
22. C. Zhang, C. Zhang, J. Qu, X. Qian, Underwater and surface aquatic locomotion of soft biomimetic robot based on bending rolled dielectric elastomer actuators, in *2023 IEEE/RSJ International Conference on Intelligent Robots and Systems (IROS)* (IEEE, 2023), pp. 4677–4682.
23. S.-J. Park, M. Gazzola, K. S. Park, S. Park, V. Di Santo, E. L. Blevins, J. U. Lind, P. H. Campbell, S. Dauth, A. K. Capulli, F. S. Pasqualini, S. Ahn, A. Cho, H. Yuan, B. M. Maoz, R. Vijaykumar, J.-W. Choi, K. Deisseroth, G. V. Lauder, L. Mahadevan, K. K. Parker, Phototactic guidance of a tissue-engineered soft-robotic ray. *Science* **353**, 158–162 (2016).
24. K. Y. Lee, S.-J. Park, D. G. Matthews, S. L. Kim, C. A. Marquez, J. F. Zimmerman, H. A. M. Ardoña, A. G. Kleber, G. V. Lauder, K. K. Parker, An autonomously swimming biohybrid fish designed with human cardiac biophysics. *Science* **375**, 639–647 (2022).
25. Z. Ren, K. Ucak, Y. Yan, M. Sitti, Undulatory propulsion at milliscale on water surface. *Adv. Sci.* **11**, 2309807 (2024).
26. Z. Zhou, R. Mittal, Computational modeling of swimming in marine invertebrates with implications for soft swimming robots. *Bioinspir. Biomim.* **15**, 046010 (2020).
27. P. Rothemund, N. Kellaris, S. K. Mitchell, E. Acome, C. Keplinger, HASEL artificial muscles for a new generation of lifelike robots—Recent progress and future opportunities. *Adv. Mater.* **33**, 2003375 (2021).
28. N. Kellaris, P. Rothemund, Y. Zeng, S. K. Mitchell, G. M. Smith, K. Jayaram, C. Keplinger, Spider-inspired electrohydraulic actuators for fast, soft-actuated joints. *Adv. Sci.* **8**, 2100916 (2021).
29. E. Leroy, R. Hinchet, H. Shea, Multimode hydraulically amplified electrostatic actuators for wearable haptics. *Adv. Mater.* **32**, 2002564 (2020).
30. I.-D. Sîrbu, D. Preninger, D. Danninger, L. Penkner, R. Schwödiauer, G. Moretti, N. Arnold, M. Fontana, M. Kaltenbrunner, Electrostatic actuators with constant force at low power loss using matched dielectrics. *Nat. Electron.* **6**, 888–899 (2023).
31. D. L. Hu, B. Chan, J. W. M. Bush, The hydrodynamics of water strider locomotion. *Nature* **424**, 663–666 (2003).
32. C. Roh, M. Gharib, Honeybees use their wings for water surface locomotion. *Proc. Natl. Acad. Sci. U.S.A.* **116**, 24446–24451 (2019).
33. X. Ji, X. Liu, V. Cacucciolo, M. Imboden, Y. Civet, A. El Haitami, S. Cantin, Y. Perriard, H. Shea, An autonomous untethered fast soft robotic insect driven by low-voltage dielectric elastomer actuators. *Sci. Robot.* **4**, eaaz6451 (2019).

34. Y. Li, B. Mabetha, J. T. Stauth, A modular switched-capacitor chip-stacking drive platform for kV-level electrostatic actuators. *IEEE J. Solid State Circuits* **58**, 3530–3543 (2023).
35. S. Demchyshyn, M. Kaltenbrunner, Ultralightweight perovskite solar cells for use in drones. *Nat. Energy* **9**, 641–642 (2024).
36. B. Cabral, L. C. Leedom, Imaging vector fields using line integral convolution, in *Proceedings of the 20th Annual Conference on Computer Graphics and Interactive Techniques SIGGRAPH '93* (Association for Computing Machinery, 1993), pp. 263–270.
37. N. Kellaris, V. G. Venkata, P. Rothemund, C. Keplinger, An analytical model for the design of Peano-HASEL actuators with drastically improved performance. *Extreme Mech. Lett.* **29**, 100449 (2019).
38. F. Hartmann, L. Penkner, D. Danninger, N. Arnold, M. Kaltenbrunner, Soft tunable lenses based on zipping electroactive polymer actuators. *Adv. Sci.* **8**, 2003104 (2021).
39. R. M. Alexander, *Principles of Animal Locomotion* (Princeton Univ. Press, 2002).
40. G. S. Triantafyllou, M. S. Triantafyllou, M. A. Grosenbaugh, Optimal thrust development in oscillating foils with application to fish propulsion. *J. Fluids Struct.* **7**, 205–224 (1993).
41. J. J. Videler, *Fish Swimming* (Chapman & Hall, 1993).
42. Y. Yadykin, V. Tenetov, D. Levin, The added mass of a flexible plate oscillating in a fluid. *J. Fluids Struct.* **17**, 115–123 (2003).
43. C. Yin, F. Wei, S. Fu, Z. Zhai, Z. Ge, L. Yao, M. Jiang, M. Liu, Visible light-driven jellyfish-like miniature swimming soft robot. *ACS Appl. Mater. Interfaces* **13**, 47147–47154 (2021).
44. C. Tang, W. Ma, B. Li, M. Jin, H. Chen, Cephalopod-inspired swimming robot using dielectric elastomer synthetic jet actuator. *Adv. Eng. Mater.* **22**, 1901130 (2020).
45. T. Yang, Y. Xiao, Z. Zhang, Y. Liang, G. Li, M. Zhang, S. Li, T.-W. Wong, Y. Wang, T. Li, Z. Huang, A soft artificial muscle driven robot with reinforcement learning. *Sci. Rep.* **8**, 14518 (2018).
46. F. Berlinger, M. Duduta, H. Gloria, D. Clarke, R. Nagpal, R. Wood, A modular dielectric elastomer actuator to drive miniature autonomous underwater vehicles, in *2018 IEEE International Conference on Robotics and Automation (ICRA)* (IEEE, 2018), pp. 3429–3435.
47. B. Peter, R. Ratnaweera, W. Fischer, C. Pradalier, R. Y. Siegwart, Design and evaluation of a fin-based underwater propulsion system, in *2010 IEEE International Conference on Robotics and Automation* (IEEE, 2010), pp. 3751–3756.

Acknowledgments: We thank K. Hjort for discussion on the propulsion mechanism. We thank S. Manoharan for assistance in 3D printing, J. Tavalante for discussion on MCU programming, and J. La Scala for assisting early development of characterization setups. We thank R. Hennig, M. Smith, and G. Grasso for assistance and advice in taking videos and photos. **Funding:** This project has received funding from the European Union's Horizon 2020 research and innovation programme under grant agreement no. 101016411 "SOMIRO." **Author contributions:** F.H. and H.S. conceptualized the work. F.H. designed and fabricated the devices, carried out the experiments, analyzed the data, derived the analytic models and scaling analysis, and created the figures and videos, with supervision from H.S. M.Ba., G.R., and F.H. conducted PIV, LIC, and underwater experiments and analyzed and visualized the data, with supervision from K.M. M.Be. designed, programmed, and characterized the electronic circuit board, with inputs from F.H. and H.S. F.H. and H.S. prepared the original draft of the manuscript. All authors reviewed and edited the manuscript. **Competing interests:** The authors declare that they have no competing interests. **Data and materials availability:** All data needed to support the conclusions of this manuscript are included in the main text or Supplementary Materials and in the Zenodo repository: https://doi.org/10.5281/zenodo.13768820.

Submitted 13 June 2024
Accepted 22 January 2025
Published 19 February 2025
10.1126/scirobotics.adr0721

Science Robotics

Highly agile flat swimming robot

Florian Hartmann, Mrudhula Baskaran, Gaetan Raynaud, Mehdi Benbedda, Karen Mulleners, and Herbert Shea

Sci. Robot. **10** (99), eadr0721. DOI: 10.1126/scirobotics.adr0721

Science Robotics (ISSN 2470-9476) is published by the American Association for the Advancement of Science. 1200 New York Avenue NW, Washington, DC 20005. The title *Science Robotics* is a registered trademark of AAAS.